This is a “preproof” accepted article for *Clay Minerals*.

This version may be subject to change during the production process.

10.1180/clm.2024.29

Ternary geopolymer with calcined halloysite: impact on mechanical properties and microstructure

Ting Yu[1,2], Baifa Zhang[1], Jiarong Chen[2], Mohammad Fahimizadeh[1], Thammaros Pantongsuk[2], Xiang Zhou[3] and Peng Yuan[1]*

[1]School of Environmental Science and Engineering, Guangdong University of Technology, Guangzhou, China

[2]CAS Key Laboratory of Mineralogy and Metallogeny/Guangdong Provincial Key Laboratory of Mineral Physics and Materials, Guangzhou Institute of Geochemistry, Institutions of Earth Science, Chinese Academy of Sciences, Guangzhou, China

[3]Jewelry Institute, Guangzhou Panyu Polytechnic, Guangzhou, China

*Email: yuanpeng@gdut.edu.cn

Abstract

As a natural clay mineral, halloysite (Hal) possesses a distinctive nanotubular morphology and surface reactivity. Hal calcined at 750°C ($Hal_{750°C}$; 0.0, 1.0, 2.0, 4.0, 6.0, 8.0 wt.%) was used to replace ground granulated blast furnace slag (GGBFS; 50.0, 49.5, 49.0, 48.0, 47.0, 46.0 wt.%) and fly ash (FA; 50.0, 49.5, 49.0, 48.0, 47.0, 46.0 wt.%) for the preparation of geopolymer in this study. The effects of the replacement ratio of $Hal_{750°C}$ on setting time, compressive strength, flexural strength, chemical composition and microstructure of the geopolymer were investigated. The results indicated that $Hal_{750°C}$ did not significantly alter the setting time. The active SiO_2 and Al_2O_3 generated from $Hal_{750°C}$ participated in the geopolymerization, forming additional geopolymer gel phases (calcium (aluminate) silica hydrate and sodium aluminosilicate hydrate), improving the 28 day compressive strength of the geopolymers. When the amount of $Hal_{750°C}$ was 2.0 wt.%, the 28 day compressive strength of the ternary (GGBFS-FA-$Hal_{750°C}$-based) geopolymer was 72.9 MPa, 34.8% higher than that of the geopolymer without the addition of $Hal_{750°C}$. The special nanotubular morphology of residual $Hal_{750°C}$ mainly acted like reinforcing fibres, supplementing the flexural strength of the geopolymer. However, excessive $Hal_{750°C}$ addition (>4.0 wt.%) reduced compressive and flexural strength values due to the low degrees of geopolymerization and the porous microstructure in the ternary geopolymer. These findings demonstrate that the appropriate addition of $Hal_{750°C}$ improved the compressive strength of geopolymers prepared using GGBFS/FA, which provides essential data for future research and supports the utilization of low-value

Hal-containing clays in geopolymer preparation.

Keywords: Alkali activation; fly ash; ground granulated blast furnace slag; nanosized tubular halloysite

The production of ordinary Portland cement (OPC) infamously consumes a large amount of energy during the calcination process and emits high levels of CO_2, SO_2 and other byproducts, resulting in severe environmental pollution (Zhang *et al.*, 2018; Mourak & Hajjaji, 2024). Geopolymers have attracted considerable research attention in recent years as potential alternatives to OPC because the manufacturing process for geopolymers consumes less energy and emits less CO_2 than OPC production. Furthermore, geopolymers exhibit excellent properties in terms of their compressive strength, thermal stability and dilatability (Duxson & Provis, 2008; Kong & Sanjayan, 2008).

Generally, materials with sufficient amounts of reactive alumina and silica are potential sources for geopolymer synthesis (Liew *et al.*, 2016; Belmokhtar *et al.*, 2018). For example, ground granulated blast furnace slag (GGBFS), fly ash (FA) and calcined clay minerals are the most commonly studied precursors for the preparation of geopolymers (Nikolov *et al.*, 2019; Ounissi *et al.*, 2020; Yu *et al.*, 2023a). However, the supply of GGBFS and FA is limited in many regions, hindering their widespread application (Antoni *et al.*, 2012; Snellings, 2016). Calcined clays have been considered as replacements for GGBFS and FA to overcome their limited supply and to help facilitate the wider application of sustainable materials such as geopolymers

(Neißer-Deiters *et al*., 2019). Therefore, more attention has been paid recently to calcined clays and, more specifically, kaolinite-rich clays for geopolymer preparation (Cardinaud *et al*., 2021). Kaolinite ($Al_2(OH)_4Si_2O_5$) is a 1:1 dioctahedral clay mineral with excellent pozzolanic activity after calcination (Belmokhtar *et al*., 2018). The addition of calcined kaolinite (metakaolin; MK) to geopolymer formulations containing GGBFS and FA can improve the mechanical properties of the geopolymer. For example, it was reported that MK accelerated the dissolution/hydrolysis of FA, while FA controlled the exothermic reaction that accompanied the alkaline dissolution/hydrolysis of calcined clay (Ogundiran & Kunmar, 2016). The synergistic effects of MK and FA led to the production of a geopolymer gel with improved compressive strength (Ogundiran & Kumar, 2016). Duan *et al*. (2016) confirmed that partial replacement of FA by MK improved the mechanical properties of the geopolymer, optimized is microstructure and reduced the level of damage from sulfate attack. In addition, the coexistence of sodium aluminosilicate hydrate (N-A-S-H) and calcium (aluminate) silica hydrate (C-(A)-S-H) gels improved the mechanical performance and durability of geopolymers (Wang *et al*., 2020; Bouha *et al*., 2022). Bernal *et al*. (2011) assessed the structural evolution of geopolymer specimens produced from alkali-activated GGBFS/MK. The results demonstrated the formation of a more polymerized C-(A)-S-H gel structure with increased Al incorporation following the addition of MK. Furthermore, the addition of MK to GGBFS increased the workability and prolonged the setting time of the alkali-activated, GGBFS-based geopolymer. This is a significant property for the application of geopolymers because a such rapid setting restrains their application in construction.

Halloysite (Hal; $Al_2(OH)_4Si_2O_5 \cdot nH_2O$, $n = 0{\sim}2$) is a naturally occurring clay mineral of the kaolin group and has a similar chemical composition to kaolinite (Çankaya *et al.*, 2024). However, Hal has a nanosized tubular structure that arises as a counterbalance to the structural stress caused by a mismatch in the apical oxygen shared between the tetrahedral SiO_4 sheet and the adjacent octahedral AlO_6 sheet in the 1:1 layer under favourable crystallization conditions and geological occurrences (Singh & Mackinnon, 1996). This unique microstructure endows Hal with a higher specific surface area and lower structural ordering than plate-like kaolinite (Fahimizadeh *et al*., 2024). Moreover, the calcination-induced changes in the structure and surface activity of Hal differ from those of kaolinite. According to Yuan *et al.* (2012), new hydroxyl groups appear on the outside surface of the Hal when calcined at temperatures of 600–900°C. The nanotubular morphology of Hal results in a greater abundance of such groups in calcined Hal compared to MK, probably resulting in different reactivities during geopolymerization. Generally, the optimal calcination temperature is different between these two minerals, as Hal is less chemically stable and requires a lower calcination temperature than kaolin (Zhang *et al.*, 2023). Moreover, the impurities present in Hal and kaolinite samples have little impact on the dehydroxylation process (Scrivener *et al.*, 2019). Previous studies have proved that calcined Hal possesses high geopolymerization activity, and the as-obtained Hal-based geopolymers could be a potential candidates for insulation materials (Barrie *et al.*, 2015; Calvino *et al.*, 2022; Kaze *et al.*, 2022; Nana *et al.*, 2024). Previous studies have confirmed that calcined Hal possesses greater geopolymerization reactivity than MK, resulting in greater Si and Al dissolution rates, faster geopolymerization rates, more compact microstructures and more rapid compressive strength development (Zhang *et al*., 2012b; Kaze *et al*., 2022; Zhang *et al*., 2023). Hence, calcined Hal can be considered a promising material for geopolymer preparation based on the above discussion.

However, few reports have explored the addition of calcined Hal to GGBFS or FA in geopolymer preparation to date. GGBFS has been frequently used in conjunction with FA for geopolymer preparation in civil engineering because the joint activation of GGBFS and FA could counterbalance the disadvantages arising from the separate alkali activation of GGBFS and FA. A alkali-activated GGBFS/FA geopolymer possessed a slow setting time and did not require elevated curing temperatures (Olivia & Nikraz, 2012). Calcined Hal possesses a special structure and high geopolymerization activity, and it can possibly act as a good filler of voids, leading to the densification of the microstructure and ultimately enhancing the mechanical properties of the geopolymer (Zhang *et al*., 2020a; Yu *et al*., 2023b). Therefore, adding calcined Hal to GGBFS/FA to prepare geopolymers may not only enhance the mechanical properties of materials but also expand the application of Hal-rich, low-value sources (e.g. rare earth tailing, granite residual soil and engineering muck; Nie *et al*., 2020; Yuan *et al*., 2022, 2024).

In this study, calcined Hal ($\text{Hal}_{750°\text{C}}$), GGBFS and FA were used as raw materials for geopolymer preparation. The role and effect of nanosized tubular Hal on the mechanical properties, chemical compositions and microstructures of ternary (GGBFS-FA-Hal$_{750°C}$-based) geopolymers were investigated. Based on the preliminary experiment, 1.0, 2.0, 4.0, 6.0 and 8.0 wt.% Hal$_{750°C}$ were used to replace GGBFS and FA during the geopolymer preparation. This manuscript provides the first report of ternary geopolymer preparation by replacing the common pozzolans of GGBFS and FA with calcined Hal. As FA and GGBFS are limited resources in some countries (Juenger *et al.*, 2019; Zunino & Scrivener, 2021), Hal is a potential and suitable alternative natural material for green construction, representing an untapped market. This study on the preparation of geopolymers from Hal is beneficial in relation to resource utilization of Hal-rich solid waste (e.g. engineering muck). The findings provide essential data for future research, which will also be conducive to utilizing low-value, Hal-containing clays in geopolymer preparation.

Materials and methods

Raw materials and specimen preparation

The raw Hal clay in this study was procured from I-Minerals, Inc., USA. The Hal powder was calcined in a muffle furnace at 750°C for 2 h, and the resulting material was denoted as Hal$_{750°C}$ as the preliminary experimental results showed that Hal calcined at 750°C exhibited the strongest geopolymerization activity compared to other temperatures (Zhang *et al.*, 2020; Yu *et al.*, 2023c). GGBFS was supplied by Shanxi Antai Group Co., Ltd, China, and FA was supplied by the Foshan Hengyi power plant, China. GGBFS and FA were directly used as obtained without any treatment.

The commercial sodium silicate (28.0 wt.% SiO_2, 8.7 wt.% Na_2O and 63.3 wt.% water) was mixed with analytical-grade NaOH pellets (purity ≥97%) to prepare the alkaline solution with a composition of $SiO_2/Na_2O = 1.5$ ($pH \geq 12$). Ultrapure water was added to adjust the sodium silicate in the alkaline activator solution to a concentration of 35%. The solutions were stored at room temperature for 1 day before use.

To better understand the influence of calcined Hal, the ratio of GGBFS to FA was fixed at 1:1. GGBFS, FA and $Hal_{750°C}$ were mixed with a mechanical stirrer (Wuxi Jianye instrument, China) for ~10 min at a low speed (140 rpm), and the mix proportions are tabulated in Table 1. After the mixing of the solid materials, the alkali activator was poured into the mixer for 120 s, mixing at a speed of 140 rpm, and then the geopolymer gel (slurry) was stirred at a speed of 285 rpm for 120 s. The liquid-to-solid (L/S) ratio was set at 0.5. The fresh geopolymer gel was cast in $20 \times 20 \times 20$ mm^3 silicon moulds for the compressive strength test and in $40 \times 40 \times 160$ mm^3 moulds for the flexural strength test, then vibrated for 1 min to allow the escape of air bubbles. The specimens were sealed in plastic bags with water under ambient conditions (~25°C) for 24 h then de-moulded. Subsequently, the specimens were sealed in plastic bags and aged under ambient conditions. The obtained specimens were denoted as 'G_{SFA}-XHal', where G_{SFA} represents geopolymer prepared by GGBFS and FA, while X represents the content of $Hal_{750°C}$. Taking G_{SFA}-2%Hal as an example, the label describes a GGBFS/FA-based geopolymer containing 2.0 wt.% $Hal_{750°C}$. Intact specimens and specimens fractured after the 28 day compressive strength test were soaked in anhydrous ethanol for 3 days to terminate the hydration process (i.e. the ethanol flush method; Zhang *et al.*, 2019, 2021). The specimens were then dried in a vacuum oven at 40°C for 24 h before being used for mercury intrusion porosimetry (MIP) measurement and scanning electron microscopy (SEM) imaging (intact specimens only). Fourier-transform infrared (FTIR) spectroscopy, X-ray diffraction (XRD) and thermogravimetry/differential thermogravimetry (TG/DTG) analyses were conducted using powder samples, with the analysed powder taken from at least 20 g of powdered intact sample for thorough representation.

Table 1. Mix compositions and element contents of the geopolymers.

Mix no.	GGBFS	FA (wt.%)	$Hal_{750°C}$ (wt.%)	L/S	Ca content (wt.%)	Si content (wt.%)	Al content (wt.%)
G_{SFA}	50.0	50.0	0.0	0.5	24.7	41.0	18.1
G_{SFA}-1%Hal	49.5	49.5	1.0	0.5	24.4	41.1	18.3
G_{SFA}-2%Hal	49.0	49.0	2.0	0.5	24.2	41.2	18.6
G_{SFA}-4%Hal	48.0	48.0	4.0	0.5	23.7	41.4	17.8
G_{SFA}-6%Hal	47.0	47.0	6.0	0.5	23.2	41.7	19.6
G_{SFA}-8%Hal	46.0	46.0	8.0	0.5	22.7	41.9	20.1

Characterization methods

The chemical composition of the raw materials was determined by X-ray fluorescence (XRF) using a wavelength-dispersive sequential scanning spectrometer (Shimadzu XRF-1800).

The particle-size distribution and specific surface area were measured using a

JL-1177 laser particle size analyser. Sodium hexametaphosphate (~1 mL with a concentration of 30%) was added to the solution to increase the dispersion of the raw materials.

Transmission electron microscopy (TEM) images were collected using a JEM-2100 TEM device operated at a 200 kV accelerating voltage. The powdered pastes were ultrasonically dispersed in ethanol for 10 min, and two droplets of the resulting dispersion were dropped onto a carbon-coated copper grid.

The specific surface area of the raw materials was determined using a Micromeritics ASAP 2020 instrument (Micromeritics Co., USA) in an N_2 physisorption analysis at liquid nitrogen temperature (–196°C). Before these measurements, the raw materials were outgassed for 12 h at a set temperature (393 K) at the degassing port.

The setting times of the geopolymer pastes were tested using a Vicat apparatus according to the ASTM C191 standard test method (ASTM C191, 2019).

A YAW-300D Compression Resistance Tester (Zhejiang) was used to determine the compressive strengths of the geopolymers aged for 7 and 28 days, with a loading rate of 500 N s^{-1}. Statistical analysis was conducted using IBM *SPSS* version 25 (IBM, USA).

A Bruker D8 Advance diffractometer (Germany) with an Ni filter and Cu-*K*α radiation ($\lambda = 0.154$ nm) was used to collect the XRD traces in the range of 3–70°2θ. The generator voltage and current were set to 40 kV and 40 mA, respectively. The scan rate was 10°2θ min^{-1}, and *JADE* software was used for analysis.

A Bruker Vertex 70V spectrometer (Germany) was used to record the FTIR spectra of the geopolymers in the range of 4000–400 cm^{-1}. Approximately 0.8 mg of the specimen powders with 80 mg potassium bromide (KBr) was mixed and pressed into a pellet, and the pellets were pressed for 1 min at a pressure of 10 MPa. More than 64 scans were collected for each measurement at a resolution of 4 cm^{-1}.

TG curves of the geopolymers were obtained using a Netzsch STA 409PC instrument, in which powdered samples were heated from 30°C to 1000°C in a corundum crucible at a heating rate of 10°C min^{-1} under an N_2 atmosphere.

SU8010 field-emission SEM and energy-dispersive X-ray spectroscopy (SEM-EDX; Hitachi, Japan) were used to collect the SEM images and EDX spectra, for which the accelerating voltages were set at 3 and 15 kV, respectively.

MIP was carried out using a MicroActive Autopore V 9500 device to measure the total porosity and to determine the critical pore size of geopolymer specimens after 28 days of curing. The contact angle (on the surface of the sample) and maximum pressure used during the measurement were 130° and 61 000 pounds per square inch, respectively.

Results and discussion

Characterization of raw materials

The chemical compositions of GGBFS, FA and $\text{Hal}_{750°\text{C}}$ (Table 2) as measured by XRF showed that the calcium (Ca) content of FA was close to 10 wt.%, which classifies FA as class F (i.e. low CaO content according to ASTM C618-19, 2019; Guo *et al*., 2021). The specific surface areas of FA, GGBFS and $\text{Hal}_{750°\text{C}}$ were 1.18, 1.71 and 25.65 m^2 g^{-1}, respectively. The D_{50} values of the GGBFS, FA and Hal$_{750°C}$ particles were 15.6, 19.6 and 23.6, respectively, based on the particle-size distribution results (Fig. 1a). The mineral compositions of GGBFS, FA and Hal$_{750°C}$ were identified according to the XRD traces presented in Fig. 1b. The broad hump at ~20–40°2θ suggested that GGBFS mainly comprised amorphous phases, and the diffraction at ~29.4°2θ was attributed to calcite, indicating that GGBFS was slightly weathered before use. A small amount of dolomite ($CaMg(CO_3)_2$; PDF#36-0426) could also be detected. Similarly, a broad hump in the 15–35°2θ range for FA was related to the amorphous phase, and the main crystalline phases of FA were quartz (SiO_2; PDF#86-1630), mullite ($Al_2Si_2O_{13}$; PDF#83-1881), anhydrite ($CaSO_4$; PDF#37-1496) and hematite (Fe_2O_3; PDF#33-0664). For Hal$_{750°C}$, only a broad reflection at ~21.1°2θ could be seen, resulting from dehydroxylation and subsequent formation of an amorphous phase (Yuan, 2016). The differences in the location of the amorphous hump were associated with the structural differences in the amorphous glasses present in the GGBFS, FA and Hal$_{750°C}$ (Ismail *et al.*, 2014; Zhang *et al.*, 2023). Figure 1c displays the FTIR spectra of the raw materials. The wavenumbers corresponding to possible vibration modes are listed in Table 3. Doublet absorption bands at 778 and 793 cm^{-1} indicated that the quartz had good crystallinity, while an amorphous phase could also be detected, which confirmed the geopolymerization of the FA (Vasić *et al.*, 2023).

Table 2. Chemical composition of GGBFS, FA and Hal$_{750°C}$.

	SiO_2	Al_2O_3	Fe_2O_3	K_2O	MgO	CaO	Na_2O	TiO_2	P_2O_5	LOI
GGBFS	30.00	15.01	1.24	0.29	9.35	38.57	0.43	0.64	0.51	0.17
FA	51.93	21.17	6.30	1.38	1.27	10.77	1.17	0.80	0.20	2.05
$Hal_{750°C}$	52.78	43.38	1.52	0.50	0.23	0.09	0.07	0.37	<0.01	0.92

LOI = loss on ignition.

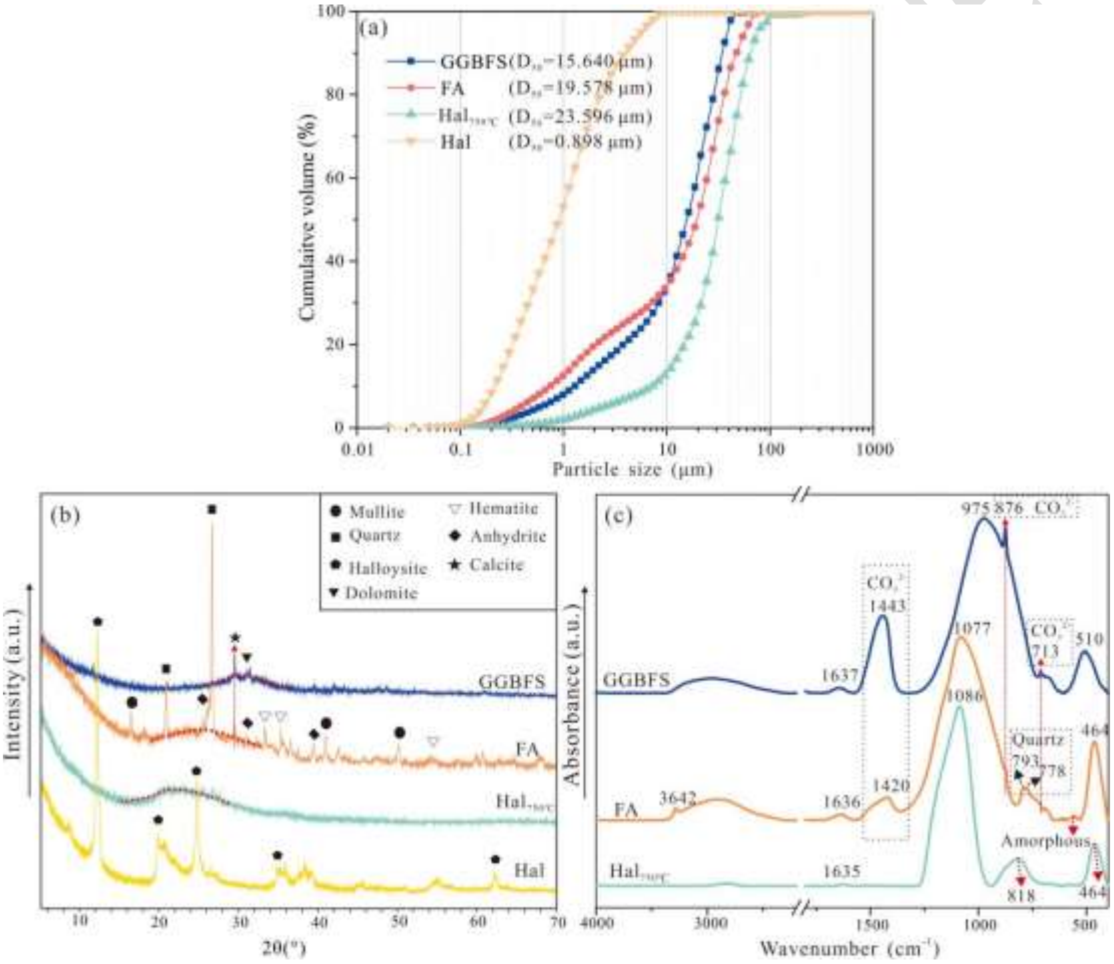

Figure 1. (a) Particle-size distribution of the raw materials, (b) XRD traces of the raw materials and (c) FTIR spectra of the raw materials.

Table 3. Wavenumbers and assignments of the FTIR peaks.

Wavenumber (cm^{-1})	Assignment	Reference
3642	Symmetric stretching vibration of the O–H of $Ca(OH)_2$	Yu *et al*. (2023c)
3450	O–H stretching vibration of water	Mathivet *et al*. (2019)
1635–1637	O–H bending vibration of water	García-Lodeiro *et al*. (2007)
1420–1443	Symmetric stretching vibration of CO_3^{2-}	García-Lodeiro *et al*. (2017)
975–1086	Symmetric stretching vibration of Si–O–Si (Al)	Zhang *et al*. (2023)
876	Out-of-plane bending vibration of CO_3^{2-}	Trezza and Lavat (2001)
818	Symmetric stretching vibration of Si–O–Si (Al)	Yuan *et al*. (2012)
778, 793	Doublet of quartz	Lee and Deventer (2003)
713	Out-of-plane bending vibration of CO_3^{2-}	Yu *et al*. (2023b)
464–510	Stretching vibration of SiO_4	Sun *et al*. (2022)

Figure 2 demonstrates the morphology of the raw components. GGBFS particles are irregular and possess angular micro-morphology (Fig. 2a). FA was mainly composed of cenospheres and plerospheres of varying sizes (Fig. 2b). $Hal_{750°C}$ possessed a tubular microstructure (Fig. 2c,d), which indicated that the tubular morphology of Hal remained largely intact after being thermally treated at the temperature of 750°C.

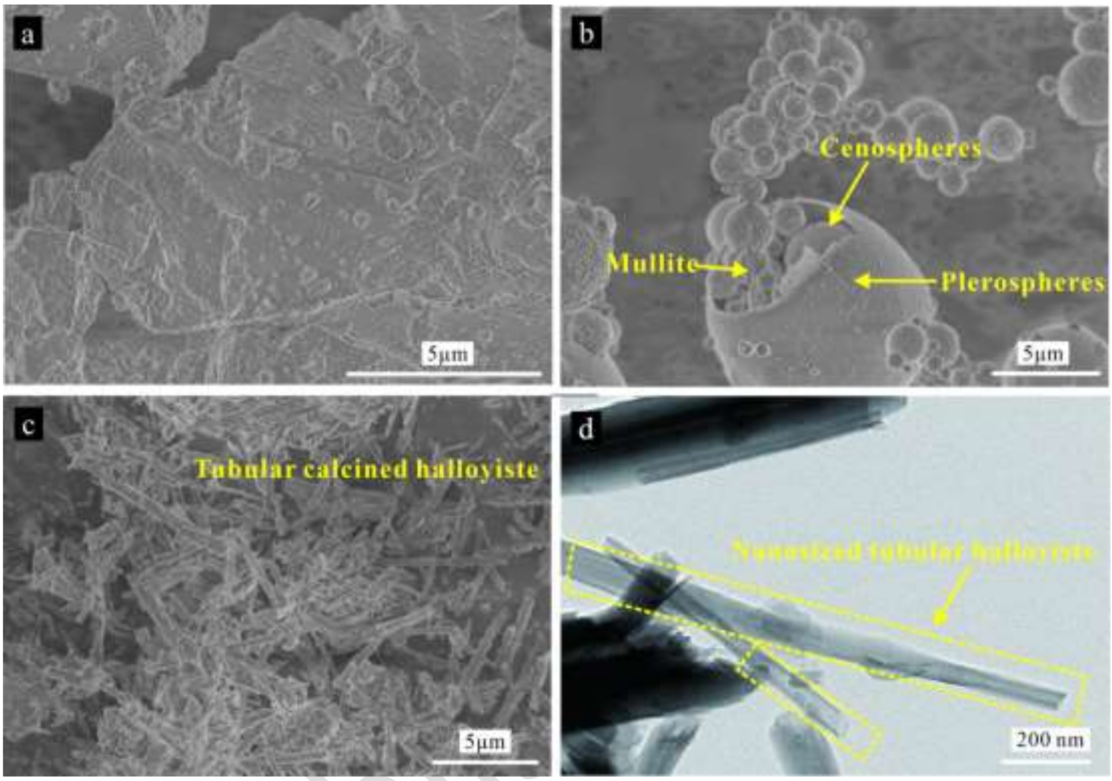

Figure 2. SEM images of the raw materials: (a) GGBFS, (b) FA and (c) $Hal_{750°C}$. (d) TEM image of Hal.

Setting times of the ternary geopolymers with $Hal_{750°C}$

Assessing the setting times of the geopolymer pastes with varying $Hal_{750°C}$ contents indicated that the proportion of $Hal_{750°C}$ slightly influenced the setting times (initial and final) in the mixtures (Fig. 3). The initial and final setting times of the control mixture were 29 and 35 min, respectively. After adding 8.0 wt.% $Hal_{750°C}$, the initial and final setting times were 28 and 34 min, respectively. It was previously reported that increased calcium content (as shown in Table 3) can shorten the initial and final setting times of geopolymers (Huseien *et al*., 2016b; Hassan *et al*., 2019; Song *et al*., 2020). In this study, replacing GGBFS and FA with $\mathrm{Hal}_{750°C}$ led to a decrease in calcium content, thus extending the setting times. In addition, Bernal *et al*. (2011) found that adding MK to the GGBFS mixture caused an increase in total setting time. However, no pronounced extension of setting time was observed in this study. This might be due to the combination of decreased calcium content and the high specific surface area of $\mathrm{Hal}_{750°C}$, resulting in the little alteration to the geopolymer setting times. However, nanosized tubular $\mathrm{Hal}_{750°C}$ possessed a high specific surface area, leading to a high water demand for geopolymer preparation (Zhang *et al*., 2014, 2021). As the water/binder ratio was kept constant, the increased amount of $\mathrm{Hal}_{750°C}$ meant that the relative availability of the alkaline solution for GGBFS and FA dissolution was reduced, resulting in less Ca release from GGBFS and FA. However, according to the study performed by Liu (2011), a high specific surface area of raw materials can hasten the geopolymerization and shorten the setting time. Therefore, the setting times of geopolymer specimens were probably shortened by increasing amounts of $\mathrm{Hal}_{750°C}$ due to the unique nanosized tubular morphology and high specific surface area of $\mathrm{Hal}_{750°C}$.

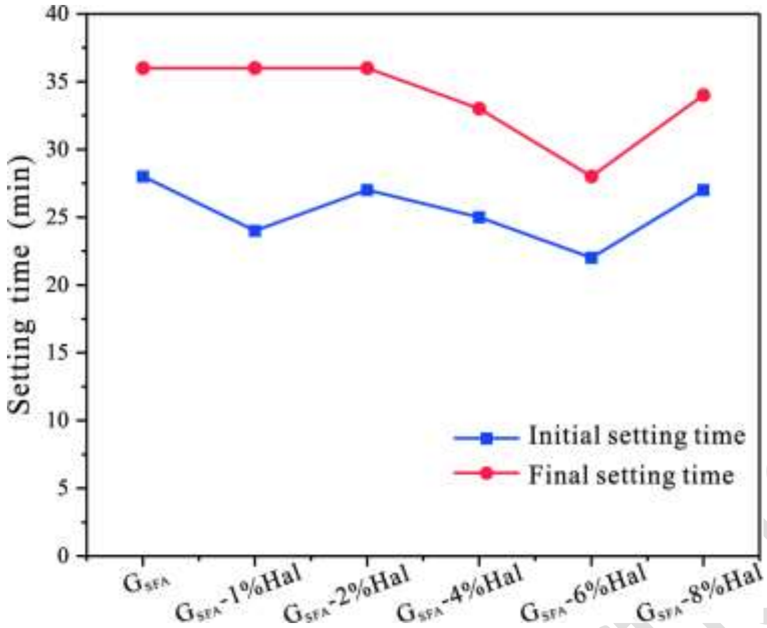

Figure 3. Initial and final setting times of geopolymer pastes with varying Hal$_{750°C}$ contents.

Compressive strengths of the ternary geopolymers with Hal$_{750°C}$

The results regarding the 28 day compressive strengths of the geopolymers with varying Hal$_{750°C}$ contents showed that G$_{SFA}$-2%Hal exhibited greater compressive strength (72.9 MPa) than the geopolymer prepared without Hal$_{750°C}$ by 16.7% (Fig. 4). This observation was mainly attributed to the addition of 2.0 wt.% Hal$_{750°C}$ providing an appropriate amount of amorphous Al_2O_3 and SiO_2 content, which was conducive to the formation of more geopolymer gel (Huseien *et al*., 2016a). Consequently, the compressive strength of geopolymer specimens was enhanced. However, the 28 day compressive strength of specimens containing >4.0 wt.% Hal$_{750°C}$ also increased, indicating that the addition of Hal$_{750°C}$ favoured the development of the later compressive strength of the geopolymer. For example, the 28 day compressive strength of the geopolymers increased from 54.1 to 59.2 MPa after 8.0 wt.% GGFS and FA was replaced with Hal$_{750°C}$. Geopolymer specimens with 0.0 and 1.0 wt.%

$\text{Hal}_{750°\text{C}}$ after 7 days of curing featured compressive strengths greater than those after 28 days of curing, which might result from the significant shrinkage of GGBFS and the low activity of FA (Neto *et al.*, 2008; Lee & Lee, 2013; Aiken *et al.*, 2021). Furthermore, the compressive strengths of geopolymers after 7 and 28 days of curing exhibited slight differences when the amount of $\text{Hal}_{750°\text{C}}$ exceeded 6.0 wt.%. This phenomenon could be due to two reasons: (1) the addition of nanotubular $\text{Hal}_{750°\text{C}}$ led to high water demand for complete geopolymerization – however, as mentioned before, the L/S ratio was fixed to 0.5 for the geopolymers, and the greater contents of $\text{Hal}_{750°\text{C}}$ (>4.0 wt.%) lowered the degree of geopolymerization and increased the porosity of the geopolymers, hence their compressive strengths decreased (Ogundiran & Kumar, 2016); and (2) less calcium silicate hydrate (C-S-H) gel was formed due to the decreased content of GGBFS. As $\text{Hal}_{750°\text{C}}$ is a calcium-free material (it either does not contain calcium or possesses only a very low calcium content), the main product of N-A-S-H, formed from geopolymerization, was less conducive to compressive strength development due to the fact that C-S-H contributes more significantly to the mechanical properties of geopolymers than N-A-S-H (Phoo-Ngernkham *et al*., 2015; Yang *et al*., 2018; Zhu *et al*., 2021).

The greater specific surface area of $\text{Hal}_{750°\text{C}}$ than MK might lead to the difference in performance of the ternary geopolymers containing FA, GGBFS and $\text{Hal}_{750°\text{C}}$ or MK. For example, in a study by Duan *et al.* (2017), geopolymer concrete prepared with 40 wt.% FA + 40 wt.% GGBFS + 20 wt.% MK, for which the L/S ratio was set to 0.30, exhibited a 28 day compressive strength of 49 MPa. Moreover, in another study, the geopolymer was prepared with 20 wt.% FA + 40 wt.% GGBFS + 40 wt.% MK, and this exhibited a 28 day compressive strength of ~33 MPa (Huang & Wang, 2021). Lv *et al*. (2024) investigated the effects of different contents of GGBFS on geopolymers prepared from FA and MK. The results indicated that the addition of GGBFS increased the compressive strength (~45 MPa) of the ternary (12 wt.% GGBFS + 28 wt.% FA + 60 wt.% MK) geopolymer when the L/S ratio was set to 0.65.

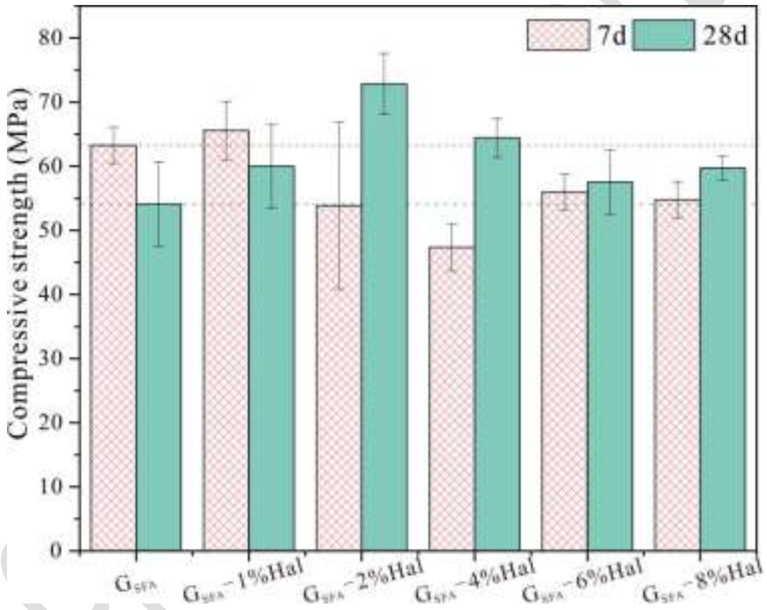

Figure 4. Compressive strengths of geopolymers with different $Hal_{750°C}$ contents.

Flexural strengths of the ternary geopolymers with $Hal_{750°C}$

Flexural strength improved after the addition of 2.0 wt.% $Hal_{750°C}$, but other replacement proportions led to loss of flexural strength (Fig. 5). G_{SFA}-2%Hal had the greatest flexural strength of 5.8 MPa after 7 days of curing, 7.4% higher than that of G_{SFA}, while the 28 day flexural strengths of G_{SFA}-2%Hal and G_{SFA} exhibited similar values (average values and error bars). These similar values might be attributed to the combination of less calcium (negative effect) and the greater geopolymerization activity of calcined Hal, which was conducive to forming more geopolymer gel (positive effect). G_{SFA}-8%Hal possessed the lowest flexural strengths of 4.0 and 4.2 MPa after 7 and 28 days of curing, respectively. Notably, the flexural strengths of G_{SFA}-2%Hal increased from 5.8 to 7.2 MPa as the aging time increased from 7 to 28 days. These results demonstrate that an appropriate content of $Hal_{750°C}$ (2.0 wt.%) in GGBFS/FA was important to improving the flexural strength of the geopolymers. A previous study reported that nanotubular Hal could be used as a reinforcing fibre to improve the mechanical properties of cement (Farzadnia *et al.*, 2013). Therefore, $Hal_{750°C}$ with geopolymerization might be conducive to the formation of geopolymer gels, while the unreacted $Hal_{750°C}$ could play a role in fibre reinforcement. Limited research has focused on the investigation of the flexural strengths MK-containing ternary geopolymers. When comparing geopolymer concrete with a cementitious material of 40 wt.% FA + 40 wt.% GGBFS + 20 wt.% MK, for which the L/S ratio was set to 0.3, the geopolymer exhibited a 28 day flexural strength of 11.3 MPa (Duan *et al.*, 2017); however, the composite was in a concrete form, therefore not being a cementitious material, hence these values being greater than those reported in the current study.

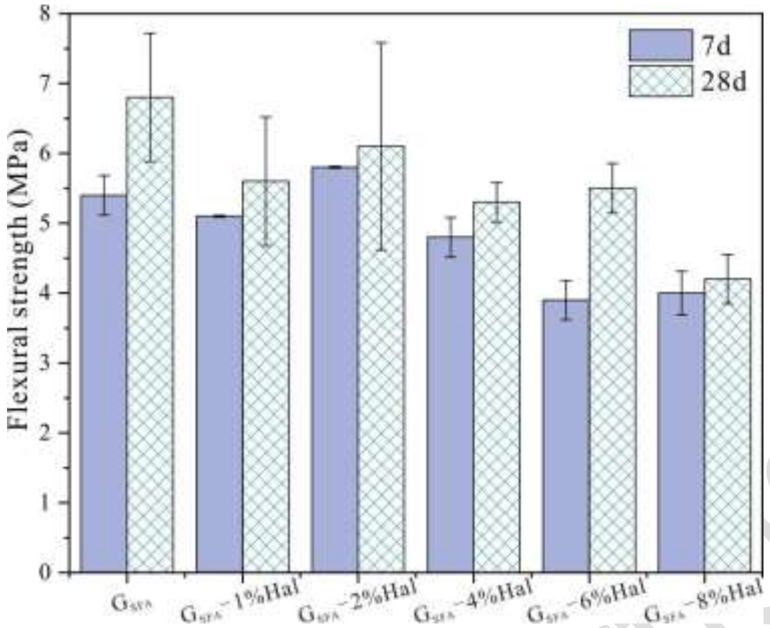

Figure 5. Flexural strengths of geopolymers with different $\mathrm{Hal}_{750°\mathrm{C}}$ contents.

Mineral phases of the ternary geopolymers with $\mathrm{Hal}_{750°\mathrm{C}}$

FTIR results of the ternary geopolymers with $\mathrm{Hal}_{750°\mathrm{C}}$

FTIR spectra of geopolymers with varying contents of $\mathrm{Hal}_{750°\mathrm{C}}$ and the wavenumbers corresponding to possible vibrational modes are shown in Fig. 6 & Table 2, respectively. All geopolymer specimens had similar broad peaks, indicating the presence of highly amorphous products (Kranzlein *et al.*, 2018). There was a major band between 1200 and 900 cm^{-1} for all geopolymer specimens, which was denoted the 'main band' and has been attributed to the Si–O–T (T = Si or Al) asymmetric stretching vibration (Lee & Deventer, 2003; Prasanphan *et al.*, 2019). This main band shifted to a higher wavenumber after incorporating the $\mathrm{Hal}_{750°\mathrm{C}}$, which might be due to the presence of the unreacted raw materials, indicating a lower degree of silicate polymerization in Si–O–Si and a lower degree of geopolymerization (Zhang *et al.*, 2012a, 2013, 2021; Aziz *et al.*, 2020). However, the higher wavenumber might also indicate that more Al participates in the geopolymerization (Hajimohammadi *et al.*, 2008; Kljajević *et al.*, 2017). The band at ~3470 cm^{-1} was assigned to the O–H stretching vibration of water (Yuan *et al.*, 2012).

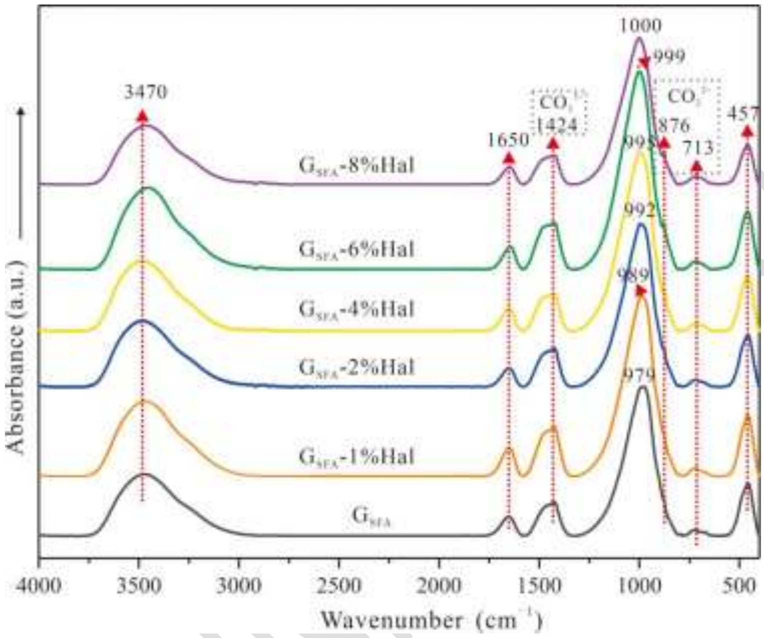

Figure 6. FTIR spectra of geopolymer with different $Hal_{750°C}$ contents.

XRD results of the ternary geopolymers with $Hal_{750°C}$

The XRD traces of geopolymers with varying contents of $Hal_{750°C}$ after 28 days of curing showed no conspicuous differences in diffraction, reflecting that the addition of $Hal_{750°C}$ did not change the mineral composition of the geopolymer specimens (Fig. 7). The broad hump at ~25°–35°2θ found in the XRD traces of the specimens indicated that the alkali-activated GGBFS/FA/$Hal_{750°C}$ products were mainly amorphous, probably C-(A)-S-H and N-A-S-H gel phases (Ling *et al.*, 2019). Moreover, the diffraction of the C-S-H crystalline phase could also be detected at

~29.5°2θ, which strongly overlaps with the reflection of calcite (Phoo-Ngernkham *et al*., 2015; Ishwarya *et al*., 2019).

The crystalline phases of mullite and quartz present in the raw FA, as well as calcite in both raw materials of GGBFS and FA, were also observed in the hardened geopolymer specimens, suggesting that such inert components had persisted in the specimens after geopolymerization, although with reduced diffraction intensity, possibly due to the dilution effect from other components, as previously reported (Bouguermouh *et al*., 2017; Sankar *et al*., 2018; Yang *et al*., 2018). The anhydrite and hematite present in raw FA were found to have disappeared, which could be attributed to the high-intensity reflection of quartz, making anhydrite and hematite difficult to detect, or perhaps both of them were dissolved during geopolymerization. New low-intensity reflections of dolomite were found at 31.4° and 41.0°2θ, possibly due to the reaction between MgO (9.35%) from GGBFS and atmospheric CO_2, according to the XRF data (Aziz *et al*., 2020).

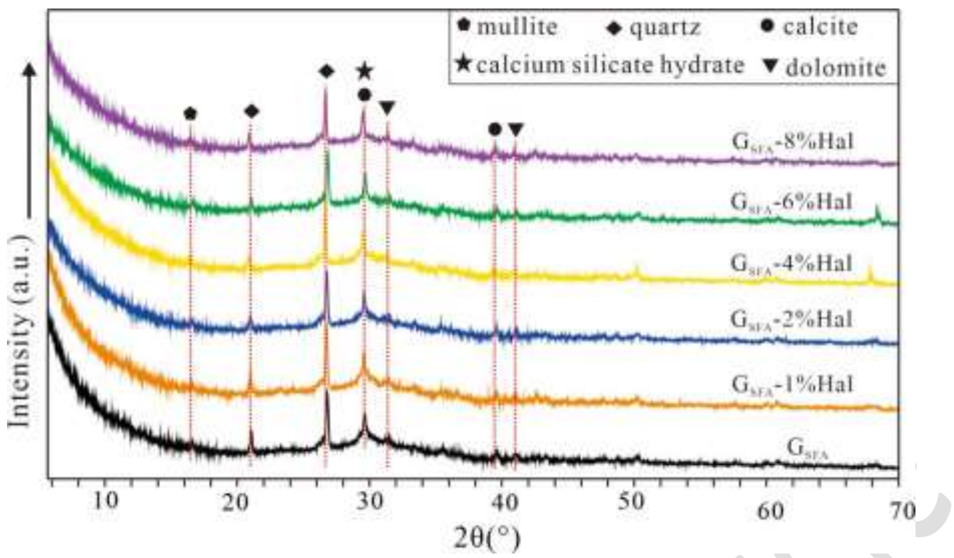

Figure 7 XRD traces of geopolymer specimens with various Hal$_{750°C}$ contents.

TG results of the ternary geopolymers with Hal$_{750°C}$

The TG analysis of geopolymer specimens with varying contents of Hal$_{750°C}$ after 28 days of curing is depicted in Fig. 8. When the specimens underwent a heating process from room temperature to 1000°C, free water loss and the decomposition of hydration products took place (Zhang *et al*., 2021). The total mass loss of geopolymer decreased with increasing Hal$_{750°C}$ content (Fig. 8a). The clear weight loss at ~100°C (Fig. 8b) was related to the evaporation of free water in the geopolymer (Abdalqader *et al*., 2016; Cong & Mei, 2021; Zhang *et al*., 2021; Li *et al*., 2022). In addition, the weight loss of geopolymer samples in this range was substantially reduced with increasing Hal$_{750°C}$ content, indicating there being less free water and C-S-H in such specimens (Huseien *et al*., 2018). Free water plays a vital role in the development of the mechanical properties of geopolymers. Water facilitates the movement of various ions derived from the dissolution of aluminosilicates, enabling the steady formation of a polymeric structure during the geopolymerization process (Zhang *et al*., 2009). The reduced availability of free water lowers the degree of geopolymerization and thus could be one of the significant drawbacks influencing the reduction of compressive and flexural strengths. Similar weight losses were observed for geopolymer specimens after the temperature increased to 150°C, 300°C and 600°C, and the chemically bound water of the geopolymers dehydrated in the 200–700°C temperature range (Bignozzi *et al*., 2014; Youmoue1 *et al*., 2020).

Calcite decomposes in the temperature range of 600–800°C (Li *et al*., 2021; Yue, 2021). However, no prominent peak was observed, implying the low contents of calcite in these specimens.

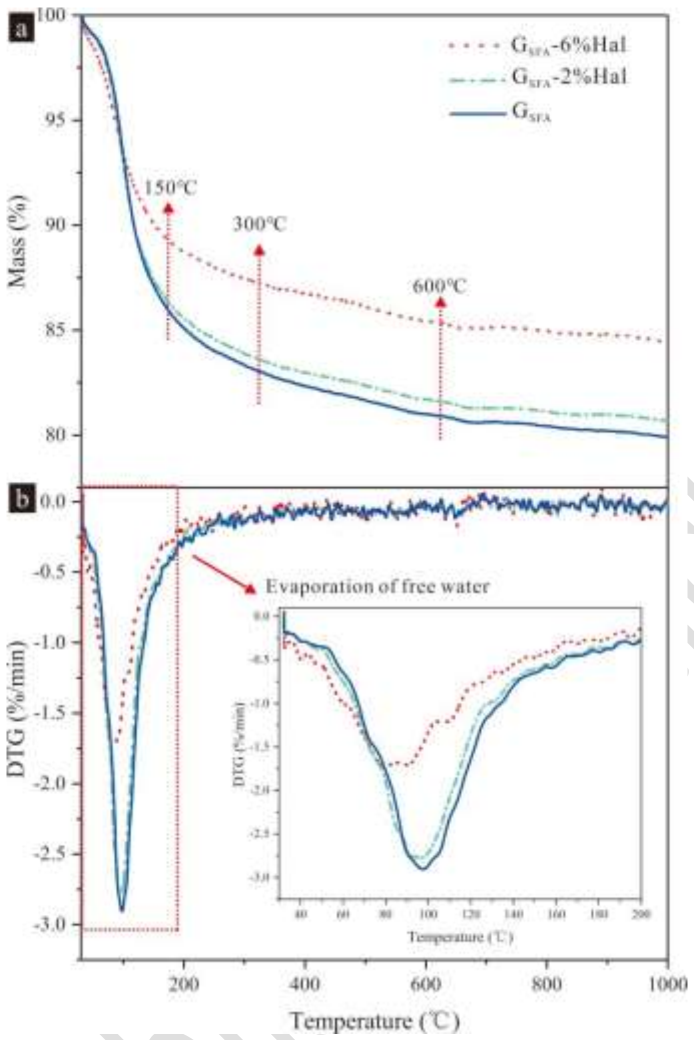

Figure 8. (a) TG curves and (b) DTG results of the geopolymers with varying $Hal_{750°C}$ contents.

Microstructure of the ternary geopolymers

SEM results of the ternary geopolymers with $Hal_{750°C}$

SEM and EDX were used to characterize the microstructure and composition of the geopolymer specimens. The microstructural developments of the various geopolymer specimens of G_{SFA}, G_{SFA}-2%Hal and G_{SFA}-6%Hal after 28 days of curing are illustrated in Figs 9–11, respectively. The remnant unreacted FA, GGBFS and $Hal_{750°C}$ could be observed, which implied a partially incomplete geopolymerization (there were still many unreacted precursors in the geopolymer matrix).

The control specimen G_{SFA} exhibited a typical geopolymer microstructure (Fig. 9), mainly comprising amorphous network gel products, pores and residual FA particles (Fig. 9a). The FA particles were dissolved through alkaline activation to form amorphous geopolymer products; however, plenty of unreacted or partially reacted FA could still be detected in the matrix (Fig. 9b). Due to the high reactivity in GGBFS, this degree of geopolymerization was higher than for FA (Nath & Sarker, 2014). Thus, there was probably no residual GGBFS left. Through EDX analysis, the main elements in the matrix near the FA particles were determined to be Na, Al and Si (Fig. 9c), signalling that the N-A-S-H gel was the main geopolymerization product. However, due to the low content of Ca in FA, the main elements in the matrix adjacent to FA were determined to be Na, Ca, Al and Si (Fig. 9d), which indicated the coexistence of N-A-S-H and C-(A)-S-H gels. These results were consistent with previous studies that have reported the main reaction products of GGBFS and FA as C-(A)-S-H and N-A-S-H gels, respectively (Chi & Huang, 2013; Marjanović *et al.*, 2015). In addition, an amorphous network gel with a porous microstructure was also found, and the EDX data indicated that this gel corresponded to a N-A-S-H gel.

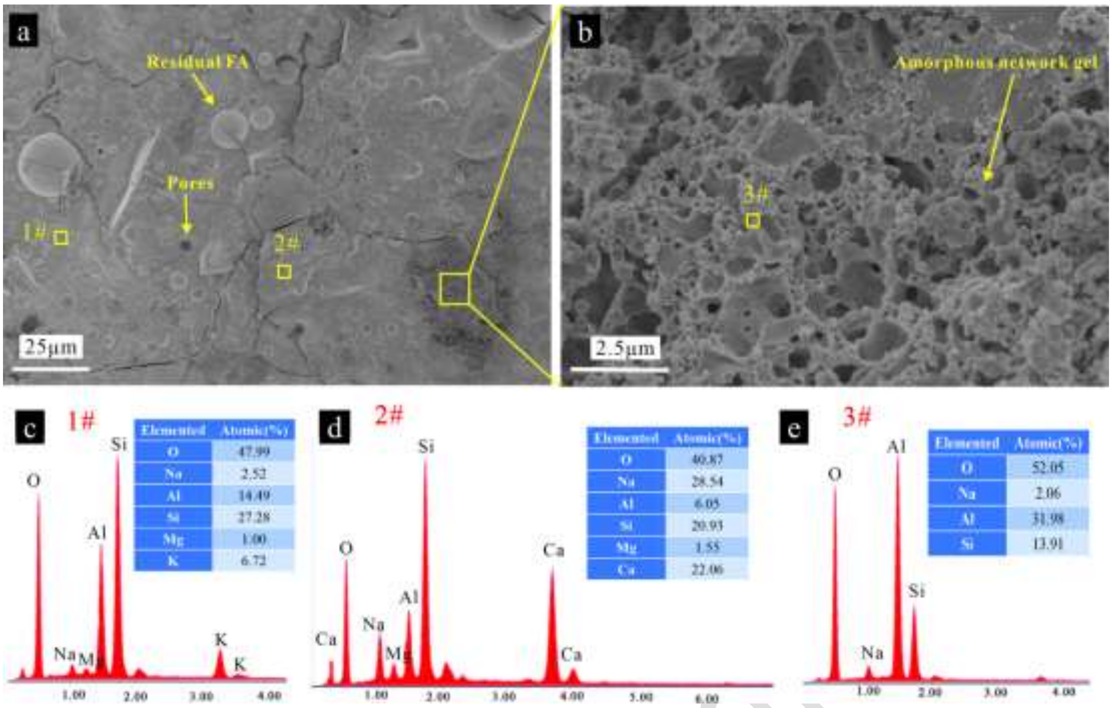

Elemented	Atomic(%)
O	47.99
Na	2.52
Al	14.49
Si	27.28
Mg	1.00
K	6.72

Elemented	Atomic(%)
O	40.87
Na	28.54
Al	6.05
Si	20.93
Mg	1.55
Ca	22.06

Elemented	Atomic(%)
O	52.05
Na	2.06
Al	31.98
Si	13.91

Figure 9. (a,b) SEM images and (c–e) EDX spectra of G_{SFA}.

More residual FA and GGBFS persisted in the matrix of G_{SFA}-2%Hal than in the control G_{SFA} specimens (Fig. 10a). The porous gel near FA was N-A-S-H (Fig. 10b,e), whereas the other geopolymer gels further from FA particles consisted of N-A-S-H and C-(A)-S-H (Fig. 10f,g). Moreover, some micro-cracks appeared in the matrix of G_{SFA}-2%Hal, possibly arising due to the uneven shrinkage force between the geopolymer gel products and the GGBFS and FA particles during the curing process (Song *et al*., 2020). Unreacted (residual) $Hal_{750°C}$ was not found in the geopolymer matrix due to its high geopolymerization reactivity or it being embedded within the matrix.

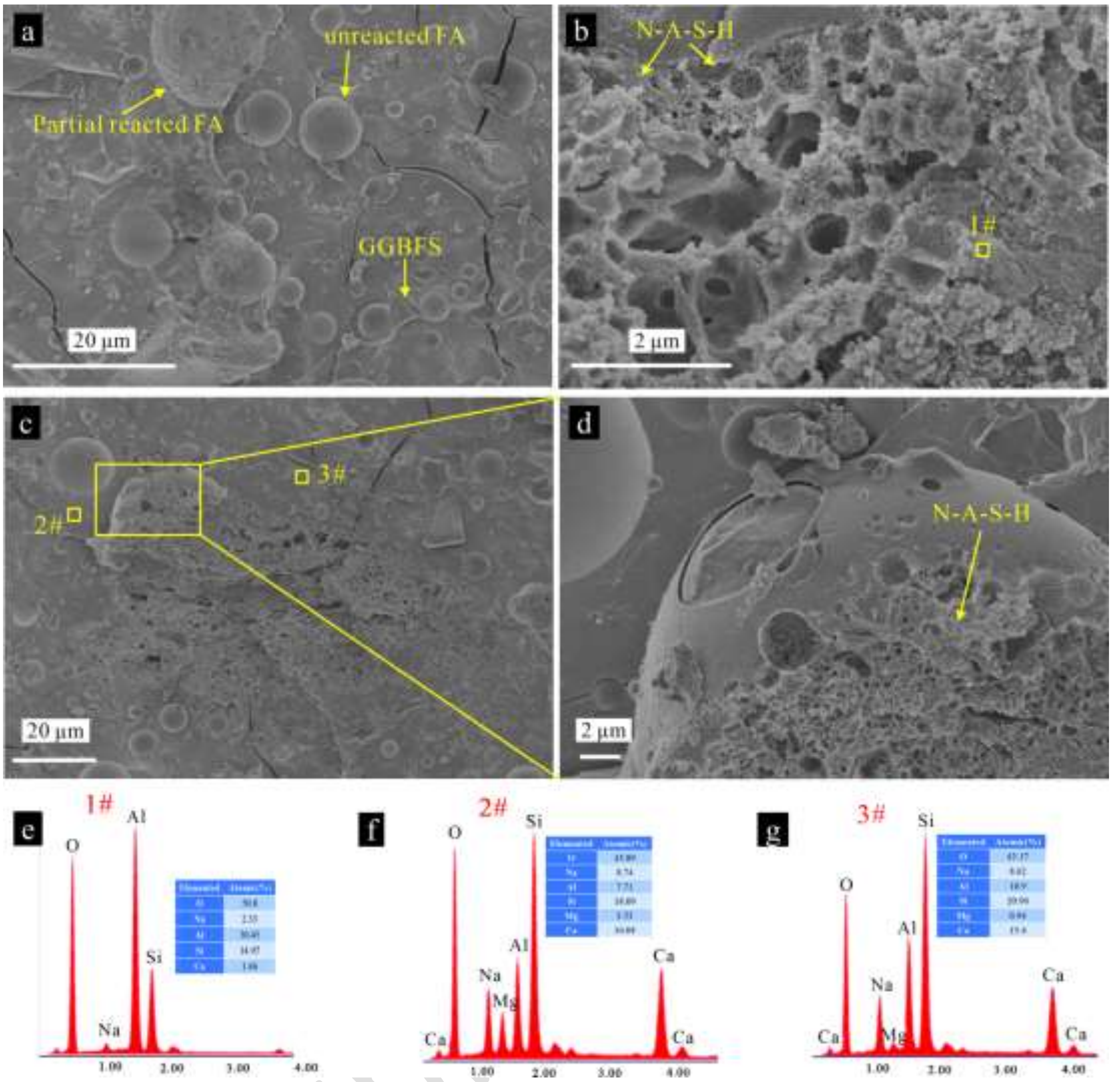

Figure 10. (a–d) SEM images and (e–g) EDX spectra of G_{SFA}-2%Hal.

Figure 11 depicts the SEM-EDX images and elemental mappings of G_{SFA}-6%Hal. The elemental mapping results showed that G_{SFA}-6%Hal consisted mainly of Na, Ca, Al, Si and Mg, and that these elements were evenly distributed within the matrix (Fig. 11a), which indicated the formation of geopolymers with N-A-S-H and C-(A)-S-H gel networks. In addition, the cenospheres, with high contents of Ca and low contents of Na, were wrapped within plerospheres (Fig. 11a), which mainly consisted of Si, Al and K. Furthermore, it was also found that the cenospheres were eroded while the plerospheres remained relatively intact.

Residual FA and GGBFS still existed within the matrices of the geopolymer samples (Fig. 11b). It should be pointed out that the generated gel products covered the surfaces of the residual $Hal_{750°C}$ particles, agglomerating them into large particles (Fig. 11c). The unreacted $Hal_{750°C}$ destroyed the homogeneity of the microstructure and subsequently produced a microporous structure in the geopolymer matrix. Therefore, the mechanical properties of the geopolymers were reduced after excessive $Hal_{750°C}$ addition. According to the EDX results, the geopolymer matrix was composed of Na, Ca, Al and Si (Fig. 11d), consistent with the mapping results.

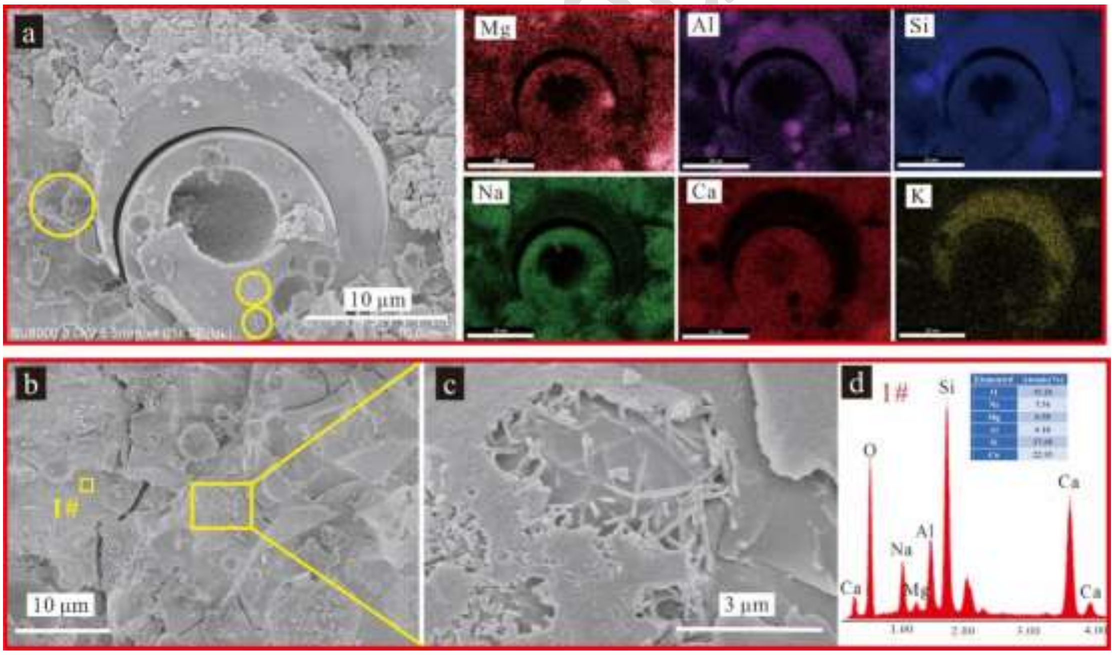

Figure 11. (a–c) SEM images with (a) element mapping and (d) EDX spectrum of G_{SFA}-6%Hal.

MIP analysis of the ternary geopolymers with $Hal_{750°C}$

The pore structure analysis of 28 day geopolymer specimens with or without the addition of $Hal_{750°C}$ as determined by MIP (Fig. 12) showed that the addition of $Hal_{750°C}$ enhanced the total geopolymer porosities (Fig. 12a), and that the pores with a diameter of <10 nm became more frequent (Fig. 12b).

The total porosity of the specimens containing $Hal_{750°C}$ increased, which resulted in lower compressive strengths compared with that of G_{SFA}. G_{SFA}-6%Hal exhibited the greatest total porosity (18.2%) compared with G_{SFA} (12.6%) and G_{SFA}-2%Hal (13.6%). The increase in total porosity may be attributed to the decreased Ca content and the transformation of C-(A)-S-H into N-A-S-H gels after adding $Hal_{750°C}$, as C-(A)-S-H gel possesses better space-filling capacity than N-A-S-H gel. In addition, the C-(A)-S-H gel could refine the micropores or cracks in geopolymerization due to its finer particle size than N-A-S-H gel (Zhu *et al.*, 2021). Thus, N-A-S-H gels contributed less to the mechanical properties of the ternary geopolymers. Furthermore, the inherent porosity of raw $Hal_{750°C}$ also contributed to the increased total porosity. However, in contrast to the porosity, G_{SFA} possessed larger amounts of pores with sizes in the range of 10–100 nm than G_{SFA}-2%Hal and G_{SFA}-6%Hal; this could be attributed to the filler effect of nanosized Hal, which refined the pore microstructures of the geopolymers.

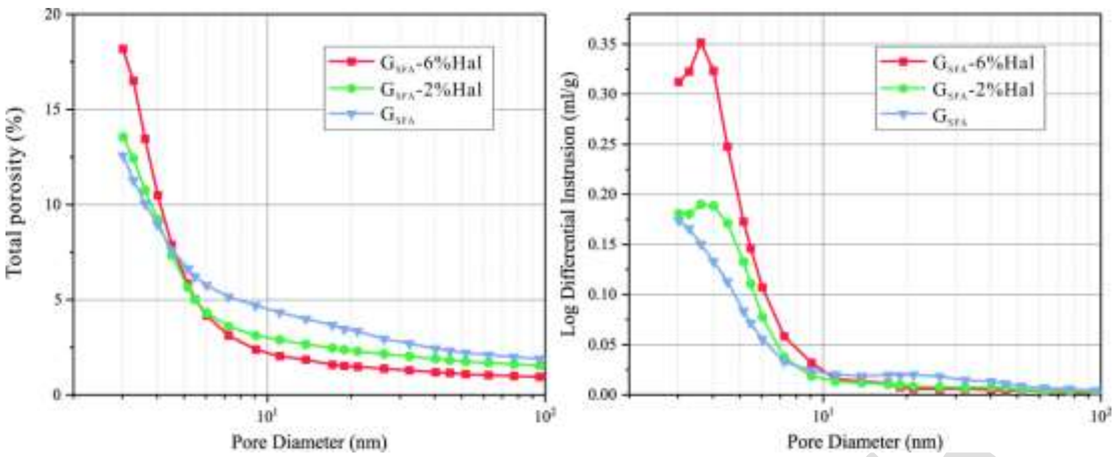

Figure 12. MIP curves of the geopolymers with various $Hal_{750°C}$ contents: (a) total porosity and (b) pore-size distribution.

Summary and conclusion

To expand the potential application of Hal-rich, low-value sources such as granite residual soil and rare earth tailings, $Hal_{750°C}$ was introduced into GGBFS/FA-based geopolymers as an active additive to produce a ternary geopolymer formulation with reduced reliance on FA and GGBFS, in consideration of the limited supply of these commonly used pozzolans. This study investigated the impacts of GGBFS/FA replacement with varying levels of $Hal_{750°C}$ on the setting times, mechanical properties, chemical compositions and microstructures of geopolymers by multi-technical characterization. The results showed that the addition of $Hal_{750°C}$ had little influence on the setting time; the primary causes of this were the decreased Ca content and the high specific surface area of $Hal_{750°C}$. The active SiO_2 and Al_2O_3 generated from $Hal_{750°C}$ participated in geopolymerization, forming additional geopolymer gels (C-(A)-S-H and N-A-S-H) and improving the compressive strengths of the geopolymers at older ages. The 28 day compressive strength of the ternary geopolymer with 2.0 wt.% $Hal_{750°C}$ was 34.8% higher than that of the $Hal_{750°C}$-free control geopolymer specimen (G_{SFA}). In contrast, excessive addition of $Hal_{750°C}$ had a detrimental effect on the mechanical properties, probably due to the agglomeration of residual $Hal_{750°C}$ on the geopolymer gel surface, resulting in a loose and porous microstructure. The impact of $Hal_{750°C}$ addition affected flexural strength and compressive strength similarly. $Hal_{750°C}$ with high geopolymerization activity was conducive to the formation of geopolymer gel phases, and residual nanosized tubular $Hal_{750°C}$ could be considered as a reinforcing fibre. Finally, applying calcined Hal in GGBFS/FA-based geopolymers at the optimum quantity is demonstrated in this study.

This study revealed key insights into the role of the clay mineral Hal in the preparation of ternary geopolymers, demonstrating the fundamental role of calcined Hal as an additive for geopolymer preparation and deepening our understanding regarding the potential of this approach while highlighting the remaining challenges in this area regarding sustainability. Given the global abundance of Hal, future research should seek to apply calcined Hal clay minerals in geopolymer preparation. More comparative studies on the application potential of low-value, Hal-containing clays, such as ion adsorption-type rare earth tailings, engineering mucks for geopolymer preparation and the durability of Hal-based geopolymers, should be conducted in future research.

Financial support

This work is supported by the National Natural Science Foundation of China (Grant Nos. 52161145405 and 423020012) and Guangdong Basic and Applied Basic

Research Foundation (No. 2023A1515012180).

Conflicts of interest

The authors declare that they have no known competing financial interests or personal relationships that could have appeared to influence the work reported in this paper.

Reference

Abdalqader A.F., Jin F. & Al-Tabbaa A. (2016) Development of greener alkali-activated cement: utilization of sodium carbonate for activating slag and fly ash mixtures. *Journal of Cleaner Production*, **113**, 66–75.

Aiken T.A., Kwasny J., Sha W. & Tong K.T. (2021) Mechanical and durability properties of alkali-activated fly ash concrete with increasing slag content. *Construction and Building Materials*, **301**, 124330.

Antoni M., Rossen J., Martirena F. & Scrivener K. (2012) Cement substitution by a combination of metakaolin and limestone. *Cement and Concrete Research*, **42**, 1579–1589.

ASTM C191 (2019) Standard test methods for time of setting of hydraulic cement by Vicat Needle. Available at https://www.astm.org/c0191-19.html

ASTM C618-19 (2019) Standard specification for coal fly ash and raw or calcined natural pozzolan for use in concrete. Available at https://www.astm.org/c0618-19.html

Aziz I.H., Abdullah M.M.A.B., Mohd Salleh M.A.A., Azimi E.A., Chaiprapa J. & Sandu A.V. (2020) Strength development of solely ground granulated blast furnace slag geopolymers. *Construction and Building Materials*, **250**, 118720.

Barrie E., Cappuyns V., Vassilieva E., Adriaens R., Hollanders S., Garcés D. *et al.* (2015) Potential of inorganic polymers (geopolymers) made of halloysite and volcanic glass for the immobilization of tailings from gold extraction in Ecuador. *Applied Clay Science*, **109–110**, 95–106.

Belmokhtar N., Ayadi H.E., Ammari M. & Allal L.B. (2018) Effect of structural and textural properties of a ceramic industrial sludge and kaolin on the hardened geopolymer properties. *Applied Clay Science*, **162**, 1–9.

Bernal S.A., Provis J., Rose V. & Gutierrez R.M.D. (2011) Evolution of binder structure in sodium silicate-activated slag–metakaolin blends. *Cement and Concrete Composites*, **33**, 46–54.

Bouguermouh K., Bouzidi N., Mahtout L., Pérez-Villarejo L. & Martínez-Cartas M.L. (2017) Effect of acid attack on microstructure and composition of metakaolin-based geopolymers: the role of alkaline activator. *Journal of Non-Crystalline Solids*, **463**, 128–137.

Bouha E.M., Bonnet S., Khelidj A., Leklou N., Froelich D., Babah I.A. *et al.* (2022) Compensation of the negative effects of micro-encapsulated phase change materials by incorporating metakaolin in geopolymers based on blast furnace slag. *Construction and Building Materials*, **314**, 125556.

Calvino M.M., Lisuzzo L., Cavallaro G., Lazzara G. & Milioto S. (2022) Halloysite based geopolymers filled with wax microparticles as sustainable building materials with enhanced thermo-mechanical performances. *Journal of Environmental Chemical Engineering*, **10**, 108594.

Çankaya N., Ünal A. & Korcan S.E. (2024) Comparison of the antimicrobial and antioxidant properties of halloysite nanotubes and organoclays as green source materials. *Clay Minerals*, **59**, 1–10.

Cardinaud G., Rozière E., Martinage O., Loukili A. & Deneele D. (2021) Calcined clay–limestone cements: hydration processes with high and low-grade kaolinite clays. *Construction and Building Materials*, **277**, 122271.

Chi M. & Huang R. (2013) Binding mechanism and properties of alkali-activated fly ash/slag mortars. *Construction and Building Materials*, **40**, 291–298.

Cong P. & Mei L. (2021) Using silica fume for improvement of fly ash/slag based geopolymer activated with calcium carbide residue and gypsum. *Construction and Building Materials*, **275**, 122171.

Duan P., Yan C. & Wei Z. (2016) Influence of partial replacement of fly ash by metakaolin on mechanical properties and microstructure of fly ash geopolymer paste exposed to sulfate attack. *Ceramics International*, **42**, 3504–3517.

Duan P., Yan C. & Wei Z. (2017) A novel water permeable geopolymer with high strength and high permeability coefficient derived from fly ash, slag and metakaolin. *Advanced Powder Technology*, **28**, 1430–1434.

Duxson P. & Provis J.L. (2008) Designing precursors for geopolymer cements. *Journal of the American Ceramic Society*, **91**, 3864–3869.

Fahimizadeh M., Wong L.W., Baifa Z., Sadjadi S., Auckloo S.A.B., Palaniandy K. *et al.* (2024) Halloysite clay nanotubes: innovative applications by smart systems. *Applied Clay Science*, **251**, 107319.

Farzadnia N., Abang Ali A.A., Demirboga R. & Anwar M.P. (2013) Effect of halloysite nano-clay on mechanical properties, thermal behavior and microstructure of cement mortars. *Cement and Concrete Research*, **48**, 97–104.

García-Lodeiro I., Fernández-Jiménez A., Blanco M.T. & Palomo A. (2008) FTIR study of the sol–gel synthesis of cementitious gels: C-S-H and N-A-S-H. *Journal of Sol–Gel Science and Technology*, **45**, 63–72.

Guo H., Zhang B., Deng L., Yuan P., Li M. & Wang Q. (2021) Preparation of high-performance silico-aluminophosphate geopolymers using fly ash and metakaolin as raw materials. *Applied Clay Science*, **204**, 106019.

Hajimohammadi A., Provis J.L. & Deventer J.S.J.V. (2008) One-part geopolymer mixes from geothermal silica and sodium aluminate. *Industrial and Engineering Chemistry Research*, **47**, 9396–9405.

Hassan A., Arif M. & Shariq M. (2019) Use of geopolymer concrete for a cleaner and sustainable environment – a review of mechanical properties and microstructure. *Journal of Cleaner Production*, **223**, 704–728.

Huang W. & Wang H. (2021) Geopolymer pervious concrete modified with granulated blast furnace slag: microscale characterization and mechanical strength. *Journal of Cleaner Production*, **328**, 129469.

Huseien G.F., Mirza J., Ismail M., Ghoshal S.K. & Ariffin M. (2016a) Effect of metakaolin replaced granulated blast furnace slag on fresh and early strength properties of geopolymer mortar. *Ain Shams Engineering Journal*, **9**, 1557–1566.

Huseien G.F., Mirza J., Ismail M. & Hussin M.W. (2016b) Influence of different curing temperatures and alkali activators on properties of GBFS geopolymer mortars containing fly ash and palm-oil fuel ash. *Construction and Building Materials*, **125**, 1229–1240.

Huseien G.F., Sam A.R.M., Mirza J., Tahir M.M., Asaad M.A., Ismail M. & Shah K.W. (2018)

Waste ceramic powder incorporated alkali-activated mortars exposed to elevated temperatures: performance evaluation. *Construction and Building Materials*, **187**, 307–317.

Ishwarya G., Singh B., Deshwal S. & Bhattacharyya S.K. (2019) Effect of sodium carbonate/sodium silicate activator on the rheology, geopolymerization and strength of fly ash/slag geopolymer pastes. *Cement and Concrete Composites*, **97**, 226–238.

Ismail I., Bernal S.A., Provis J.L., Nicolas R.S., Hamdan S. & Deventer J.V. (2014) Modification of phase evolution in alkali-activated blast furnace slag by the incorporation of fly ash. *Cement and Concrete Composites,* **45**, 125–135.

Juenger M.G.G., Snellings R. & Bernal S.A. (2019) Supplementary cementitious materials: new sources, characterization, and performance insights. *Cement and Concrete Research*, **122**, 257–273.

Kaze C.R., Nana A., Lecomte-Nana G.L., Deutou J.G.N., Kamseu E., Melo U.C. *et al.* (2022) Thermal behaviour and microstructural evolution of metakaolin and meta-halloysite-based geopolymer binders: a comparative study. *Journal of Thermal Analysis and Calorimetry*, **147**, 2055–2071.

Kljajević L.M., Nenadović S.S., Nenadović M.T., Bundaleski N.K., Todorović B.Ž., Pavlović V.B. & Rakočević Z.L. (2017) Structural and chemical properties of thermally treated geopolymer samples. *Ceramics International*, **43**, 6700–6708.

Kong D. & Sanjayan J.G. (2008) Damage behavior of geopolymer composites exposed to elevated temperatures. *Cement and Concrete Composites*, **30**, 986–991.

Kranzlein E., Pollmann H. & Krcmar W. (2018) Metal powders as foaming agents in fly ash based geopolymer synthesis and their impact on the structure depending on the Na/Al ratio. *Cement* *and Concrete Composites*, **90**, 161–168.

Lee N.K. & Lee H.K. (2013) Setting and mechanical properties of alkali-activated fly ash/slag concrete manufactured at room temperature. *Construction and Building Materials,* **47**, 1201–1209.

Lee W. & Deventer J.V. (2003) Use of infrared spectroscopy to study geopolymerization of heterogeneous amorphous aluminosilicates. *Langmuir*, **19**, 8726–8734.

Li M., Luo R., Qin L., Liu H., Duan P., Jing W. *et al.* (2022) High temperature properties of graphene oxide modified metakaolin based geopolymer paste. *Cement and Concrete Composites*, **125**, 104318.

Li Y., Li J., Cui J., Shan Y. & Niu Y. (2021) Experimental study on calcium carbide residue as a combined activator for coal gangue geopolymer and feasibility for soil stabilization. *Construction and Building Materials*, **312**, 125465.

Liew Y.M., Heah C.Y., Mohd M.A.B. & Kamarudin H. (2016) Structure and properties of clay-based geopolymer cements: a review. *Progress in Materials Science*, **83**, 595–629.

Ling Y., Wang K., Li W., Shi G. & Lu P. (2019) Effect of slag on the mechanical properties and bond strength of fly ash-based engineered geopolymer composites. *Composites Part B: Engineering*, **164**, 747–757.

Liu D.M. (2011) Research on application of phosphorus slag in cement. *Applied Mechanics and Materials*, **117–119**, 1437–1440.

Lv Y.G., Pan B., Han W.W., Qiao J., Zhang B., Zhang J.H. & Peng H. (2024) Carbonation resistance of fly ash–metakaolin-based geopolymer pastes regulated by slag and carbide slag. *Journal of Sustainable Cement-Based Materials*, **13**, 1538–1511.

Marjanović N., Komljenović M., Baščarević Z., Nikolić V. & Petrović R. (2015) Physical–mechanical and microstructural properties of alkali-activated fly ash–blast furnace slag blends. *Ceramics International*, **41**, 1421–1435.

Mathivet V., Jouin J., Gharzouni A., Sobrados I., Celerier H., Rossignol S. & Parlier M. (2019) Acid-based geopolymers: understanding of the structural evolutions during consolidation and after thermal treatments. *Journal of Non-Crystalline Solids*, **512**, 90–97.

Mourak A. & Hajjaji M. (2024) Moroccan heated clay-based geopolymer reinforced with date palm cellulose: microstructure characterization and mechanical/physical properties. *Clay Minerals*, **59**, 50–62.

Nana A., Tchummegne I.K., Tome S., Adesina A., Alomayri T., Singla R. *et al.* (2024) Comparison of feldspar and meta-halloysite geopolymers by alkaline and acidic activation. *Construction and Building Materials*, **424**, 135953.

Nath P. & Sarker P.K. (2014) Effect of GGBFS on setting, workability and early strength properties of fly ash geopolymer concrete cured in ambient condition. *Construction and Building Materials*, **66**, 163–171.

Neißer-Deiters A., Scherb S., Beuntner N. & Thienel K.C. (2019) Influence of the calcination temperature on the properties of a mica mineral as a suitability study for the use as SCM. *Applied Clay Science*, **179**, 105168.

Neto A.A.M., Cincotto M.A. & Repette W. (2008) Drying and autogenous shrinkage of pastes and mortars with activated slag cement. *Cement and Concrete Research*, **38**, 565–574.

Nie W., Zhang R., He Z., Zhou J., Wu M., Xu Z. *et al.* (2020) Research progress on leaching technology and theory of weathered crust elution-deposited rare earth ore. *Hydrometallurgy*,

193, 105295.

Nikolov A., Nugteren H., Petrov O., Rostovsky I., Petrova T. & Delcheva Z. (2019) Synthesis of natural zeolite agglomerates: clinoptilolite-based geopolymers through aluminate activation. *Clay Minerals*, **54**, 393–400.

Ogundiran M.B. & Kumar S. (2016) Synthesis of fly ash-calcined clay geopolymers: reactivity, mechanical strength, structural and microstructural characteristics. *Construction and Building Materials*, **125**, 450–457.

Olivia M. & Nikraz H. (2012) Properties of fly ash geopolymer concrete designed by Taguchi method. *Materials and Design*, **36**, 191–198.

Ounissi C., Mahmoudi S., Valentini L., Bennour A., Garbin E., Artioli G. & Montacer M. (2020) Potential use of Kebilian clay reserves (southern Tunisia) for the production of geopolymer materials. *Clay Minerals*, **55**, 101–111.

Phoo-Ngernkham T., Maegawa A., Mishima N., Hatanaka S. & Chindaprasirt P. (2015) Effects of sodium hydroxide and sodium silicate solutions on compressive and shear bond strengths of FA–GBFS geopolymer. *Construction and Building Materials*, **91**, 1–8.

Prasanphan S., Wannagon A., Kobayashi T. & Jiemsirilers S. (2019) Reaction mechanisms of calcined kaolin processing waste-based geopolymers in the presence of low alkali activator solution. *Construction and Building Materials*, **221**, 409–420.

Sankar K., Stynoski P., Al-Chaar G.K. & Kriven W.M. (2018) Sodium silicate activated slag-fly ash binders: part I – processing, microstructure, and mechanical properties. *Journal of the American Ceramic Society*, **101**, 2228–2244.

Scrivener K., Zunino F., Avet F., Ston J., Maraghechi H., Hanpongpun W. & Favier A. (2019)

Impacting factors and properties of limestone calcined clay cements (LC^3). *Green Material*, **7**, 3–14.

Snellings R. (2016) Assessing, understanding and unlocking supplementary cementitious materials. *RILEM Technical Letters*, **1**, 50–55.

Song W., Zhu Z., Pu S., Wan Y. & Hu L. (2020) Multi-technical characterization and correlations between properties of standard cured alkali-activated high-calcium FA binders with GGBS as additive. *Construction and Building Materials*, **241**, 117996.

Sun X., Liu J., Qiu J., Wu P. & Zhao Y. (2022) Alkali activation of blast furnace slag using a carbonate-calcium carbide residue alkaline mixture to prepare cemented paste backfill. *Construction and Building Materials*, **320**, 126234.

Trezza M.A. & Lavat A.E. (2001) Analysis of the system $3CaO·Al_2O_3$–$CaSO_4·2H_2O$–$CaCO_3$–H_2O by FT-IR spectroscopy. *Cement and Concrete Research*, **31**, 869–872.

Vasić M.V., Jantunen H., Mijatović N., Nelo M. & Muñoz Velasco P. (2023) Influence of coal ashes on fired clay brick quality: random forest regression and artificial neural networks modeling. *Journal of Cleaner Production*, **407**, 137153.

Wang A., Zheng Y., Zhang Z., Liu K., Li Y., Shi L. & Sun D. (2020) The durability of alkali-activated materials in comparison with ordinary portland cements and concretes: a review. *Engineering*, **6**, 695–706.

Yang T., Zhu H., Zhang Z., Gao X., Zhang C. & Wu Q. (2018) Effect of fly ash microsphere on the rheology and microstructure of alkali-activated fly ash/slag pastes. *Cement and Concrete Research*, **109**, 198–207.

Yu T., Chen J., Guo H., Zhang B., He X., Zheng A. *et al.* (2023a) Mechanical properties and microstructure of ground granulated blast furnace slag-based geopolymer reinforced with polyvinyl alcohol fibers. *Journal of Material Cycles and Waste Management*, **25**, 1719–1731

Yu T., Zhang B., Guo H., Wang Q., Liu D., Chen J. & Yuan P. (2023b) Calcined nanosized tubular halloysite for the preparation of limestone calcined clay cement (LC^3). *Applied Clay Science*, **232**, 106795.

Yu T., Zhang B., Yuan P., Guo H., Liu D., Chen J. *et al.* (2023c) Optimization of mechanical performance of limestone calcined clay cement: effects of calcination temperature of nanosized tubular halloysite, gypsum content, and water/binder ratio. *Construction and Building Materials*, **389**, 131709.

Yuan B., Chen W., Zhao J., Li L., Liu F., Guo Y. & Zhang B. (2022) Addition of alkaline solutions and fibers for the reinforcement of kaolinite-containing granite residual soil. *Applied Clay Science*, **228**, 106644.

Yuan B., Liang J., Li X., Zhang B., Luo Q., Sabri S.M.M. *et al.* (2024) Sustainable utilization of clay minerals-rich engineering muck *via* alkali-activation: optimization of pore structure by thermal treatment. *Applied Clay Science*, **258**, 107491.

Yuan P. (2016) Thermal-treatment-induced deformations and modifications of halloysite. Pp. 137–166 in: *Nanosized Tubular Clay Minerals: Halloysite and Imogolite* (P. Yuan, A. Thill & F. Bergaya, editors). Developments in Clay Science, Vol. 7. Elsevier, Amsterdam, The Netherlands.

Yuan P., Tan D., Annabi-Bergaya F., Yan W., Fan M., Liu D. & He H. (2012) Changes in structure, morphology, porosity, and surface activity of mesoporous halloysite nanotubes under heating. *Clays and Clay Minerals*, **60**, 561–573.

Yue C. (2021) Low-carbon binders produced from waste glass and low-purity metakaolin for cemented paste backfill. *Construction and Building Materials*, **312**, 125443.

Zhang B., Guo H., Yuan P., Li Y., Wang Q., Deng L. & Liu D. (2020) Geopolymerization of halloysite *via* alkali-activation: dependence of microstructures on precalcination. *Applied Clay Science*, **185**, 105375.

Zhang B., Yu T., Guo H., Chen J., Liu Y. & Yuan P. (2023) Effect of the SiO_2/Al_2O_3 molar ratio on the microstructure and properties of clay-based geopolymers: a comparative study of kaolinite-based and halloysite-based geopolymers. *Clays and Clay Minerals*, **70**, 882–902.

Zhang B., Yuan P., Guo H., Deng L., Li Y., Li L. *et al.* (2021) Effect of curing conditions on the microstructure and mechanical performance of geopolymers derived from nanosized tubular halloysite. *Construction and Building Materials*, **268**, 121186.

Zhang P., Zheng Y., Wang K. & Zhang J. (2018) A review on properties of fresh and hardened geopolymer mortar. *Composites Part B: Engineering*, **152**, 79–95.

Zhang Z., Hao W., Zhu Y., Reid A. & Bullen F. (2014) Using fly ash to partially substitute metakaolin in geopolymer synthesis. *Applied Clay Science*, **88–89**, 194–201.

Zhang Z., Provis J.L., Wang H., Bullen F. & Reid A. (2013) Quantitative kinetic and structural analysis of geopolymers. Part 2. Thermodynamics of sodium silicate activation of metakaolin. *Thermochimica Acta*, **565**, 163–171.

Zhang Z., Wang H., Provis J.L., Bullen F., Reid A. & Zhu Y. (2012a) Quantitative kinetic and structural analysis of geopolymers. Part 1. The activation of metakaolin with sodium hydroxide. *Thermochimica Acta*, **539**, 23–33.

Zhang Z., Wang H., Yao X. & Zhu Y. (2012b) Effects of halloysite in kaolin on the formation and properties of geopolymers. *Cement and Concrete Composites*, **34**, 709–715.

Zhang Z., Xiao Y., Huajun Z. & Yue C. (2009) Role of water in the synthesis of calcined kaolin-based geopolymer. *Applied Clay Science*, **43**, 218–223.

Zhang Z., Zhu Y., Zhu H., Zhang Y., Provis J.L. & Wang H. (2019) Effect of drying procedures on pore structure and phase evolution of alkali-activated cements. *Cement and Concrete Composites*, **96**, 194–203.

Zhu H., Liang G., Li H., Wu Q. & Hua S. (2021) Insights to the sulfate resistance and microstructures of alkali-activated metakaolin/slag pastes. *Applied Clay Science*, **202**, 105968.

Zunino F. & Scrivener K. (2021) The reaction between metakaolin and limestone and its effect in porosity refinement and mechanical properties. *Cement and Concrete Research*, **140**, 106307.